Research Article Vol. 32, No. 23 / 4 Nov 2024 / Optics Express 40990
Optics EXPRESS

Characterizing post-compression of mJ-level ultrafast pulses via loose focusing in a gas cell

FENGLING ZHANG,[1,2] ANTONIOS PELEKANIDIS,[1,2] AUGUSTAS KARPAVICIUS,[1,2] MATTHIAS GOUDER,[1,2] JACOB SEIFERT,[1,2] KJELD EIKEMA,[1,2] AND STEFAN WITTE[1,2,*]

[1]*Advanced Research Center for Nanolithography, Science Park 106, 1098 XG, Amsterdam, The Netherlands*
[2]*Department of Physics and Astronomy, Vrije Universiteit, De Boelelaan 1105, 1081 HV Amsterdam, The Netherlands*
[*]*witte@arcnl.nl*

Abstract: The ability to generate high-intensity ultrashort laser pulses is a key driver for advancing the strong-field physics and its applications. Post-compression methods aim to increase the peak intensity of amplified laser pulses via spectral broadening through self-phase modulation (SPM), followed by temporal pulse compression. However, other unavoidable nonlinear self-action effects, which typically occur parallel to SPM, can lead to phase distortions and beam quality degradation. Here we study the ability to compress high-energy pulses by loose focusing in a noble gas to induce nonlinear spectral broadening, while limiting unwanted nonlinear effects such as self-focusing. We introduce ptychographic wavefront sensor and FROG measurements to identify the regimes that optimize pulse compression while maintaining high beam quality. Using a 700 mbar argon-filled double-pass-based scheme, we successfully compress 2 mJ, 170 fs, 1030 nm laser pulses to ~35 fs, achieving 90% overall flux efficiency and excellent stability. This work provides guidelines for optimizing the compressed pulse quality and further energy scaling of double-pass-based post-compression concepts.

1. Introduction

High-intensity femtosecond laser pulses are crucial for strong field physics and its applications [1]. Amplifying ultrashort pulses and shortening pulse duration represent a major challenge [2]. Among the ultrashort high-intensity lasers used in strong-field physics, Titanium:sapphire (Ti:Sa) [3] lasers are notable for their broad bandwidth and high peak intensity. In contrast, ytterbium (Yb) ion-doped lasers [4,5] can achieve very average power and pulse energy but typically have narrower bandwidths, which limited their initial impact on high-intensity applications until the introduction of post-compression techniques. Two methods are commonly employed to achieve such pulse compression at high peak intensity and average power: optical parametric chirped-pulse amplification (OPCPA) and nonlinear-propagation-based post-compression. OPCPA offers a method to amplify ultra-broadband pulses because of its extreme phase-matching bandwidths, even when pumped by narrowband but high-energy laser pulses [1,6]. On the other hand, post-compression methods [7–10] broaden the spectral width of the high-power pulses [11] through nonlinear interactions during propagation through a medium. Such post-compression methods are particularly appealing due to their high efficiency reaching beyond 95% [12].

Post-compression methods employ nonlinear self-action effects that occur when high-intensity pulses travel through a medium, leading to spectral broadening via self-phase modulation (SPM), as shown in Fig. 1(a). As the spectral phase accumulated during SPM is well-controlled and typically quadratic, subsequent dispersion compensation can effectively eliminate the pulse chirp, thereby shortening the pulse duration. A related nonlinear effect that generally occurs in parallel to SPM is self-focusing (Fig. 1(b)), leading to spatial wavefront changes and ultimately beam quality degradation [13,14]. Broadening the spectrum while also minimizing the self-focusing

#539655 https://doi.org/10.1364/OE.539655
Journal © 2024 Received 19 Aug 2024; revised 27 Sep 2024; accepted 14 Oct 2024; published 25 Oct 2024

Optics EXPRESS

effect poses a significant challenge. Currently, various efficient post-compression methods have been demonstrated for millijoule-level pulses, especially hollow-core fibers [7,15–17], single [14] or multiple plates [8,17,18], and multi-pass cells (MPC) [9,19–21]. Hollow-core fibers, filled with noble gases as the nonlinear medium, limit the influence of self-focusing as the beam propagates in a waveguide. Towards higher average power and pulse energy, precise control over the beam pointing and spatial properties are necessary to prevent fiber damage. Multi-plate setups are compact and efficient, but typically operate in a narrow designed optical parameters window with specific pulse conditions. The MPC relies on sequential nonlinear interactions at the focus of an optical cavity, typically a Herriot cell design [20]. Such an approach is scalable to high energies and maintains spatial properties through the cavity mode filtering, but does require careful design and input mode matching for a given nonlinearity.

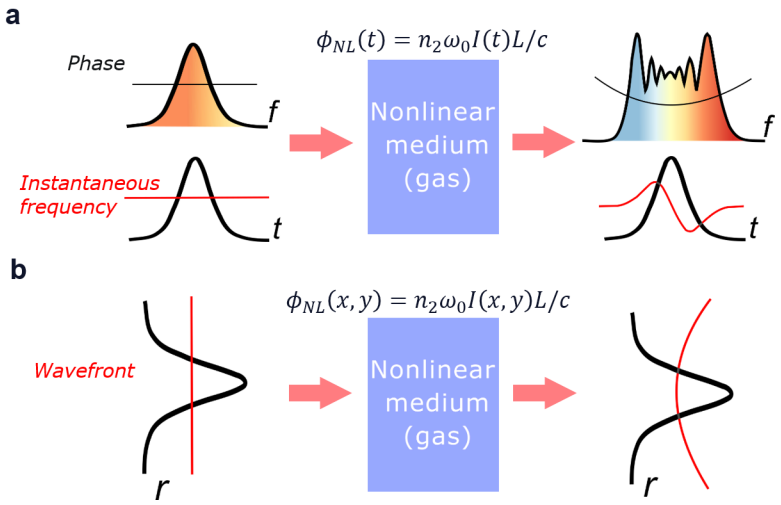

Fig. 1. Nonlinear processes that occur when a high-intensity laser beam propagates through a medium with an intensity-dependent refractive index. a) Self-phase modulation, leading to a time-dependent phase variation and subsequent spectral broadening. b) Self-focusing, leading to a spatial phase variation that influences beam propagation.

Recently, various approaches have been explored to compress pulses using hybrid MPC and multiple plates [22,23], aiming to better control the respective nonlinear effects. A specifically interesting approach is the CASCADE concept [24], which uses loose focusing in an extended gas cell to improve the ratio between self-phase-modulation and self-focusing. This approach can be efficient and robust to alignment variations, and can operate over a range of input energies.

In this work, we report on a robust double-pass setup with limited self-focusing effect for pulse compression of mJ-level, 170 fs Yb ion-doped laser pulses down to 37 fs with 90% overall efficiency, following the CASCADE concept. Each pass involves focusing into an argon gas cell to induce nonlinear spectrum broadening, followed by applying chirped-mirror-based compressor to shorten the pulse duration. We achieve over five-fold pulse compression factors after only two passes, while maintaining good spatial beam properties. In particular, we study the temporal and spatial properties of the compressed pulses in a phase-resolved way, over a wide range of gas pressures to control the amount of nonlinear interaction. The temporal pulse properties are measured using second-harmonic frequency-resolved optical gating (SHG-FROG). For spatial characterization, we use ptychographic wavefront sensing [25–27] at different wavelengths across the pulse spectrum. Using numerical pulse propagation methods, we retrieve the spatiospectral properties of the beam around a focus. This approach allows the identification of optimal working conditions for the pulse compression system. By retrieving high-resolution quantitative data at

Optics EXPRESS

specific working conditions, we can design scaling pathways towards higher pulse energy and shorter pulse duration more reliably.

2. Processes resulting from the intensity-dependent refractive index

Self-phase modulation occurs when a high-intensity light beam modifies the optical properties of a material, giving rise to an intensity-dependent nonlinear refractive index. The refractive index $n(x, y, z_0; t)$ in the presence of this type of nonlinearity at z_0 along the propagation z-direction can be written as

$$n(x, y, z_0; t) = n_0 + n_2 I(x, y, z_0; t) \tag{1}$$

where n_0 is the linear refractive index, n_2 is the nonlinear refractive index (positive value in our case) of the medium, and the intensity of the light $I(x, y, z_0; t) = 2n_0\epsilon_0 c|\widetilde{A}(x, y, z_0; t)|^2$ contributes to both spatial (x, y) and temporal t changes in the refractive index ($\widetilde{A}$ is the spatially slowly field amplitude). The effect of this nonlinear interaction is to add a propagation-dependent phase, given by:

$$\phi_{NL}(x, y; t) = -\frac{n_2\omega_0}{c}\int_0^L I(x, y, z; t)dz = -n_2 I(x, y; t)\omega_0 L/c \tag{2}$$

where ω_0 is the center angular frequency of the optical pulse, c is the speed of light, and L is the propagation distance. The phase $\phi_{NL}(x, y; t)$ is also commonly referred to as the B-integral [9,19,20,24,28]. The spectral content of the propagated pulse $S(\omega)$ can be described by its energy spectrum:

$$S(\omega) = |\int_{-\infty}^{\infty}\widetilde{A}(t)e^{-i\omega_0 t - i\phi_{NL}(t)}e^{i\omega t}dt|^2. \tag{3}$$

The temporal pulse shape $I(t)$ leads to a time-dependent phase $\phi_{NL}(t)$, which results in the generation of new frequencies to the spectrum $S(\omega)$. This is the process of self-phase modulation, which can be intuitively described by introducing the instantaneous frequency $\omega(t) = \omega_0 + \delta\omega(t)$, where the variation $\delta\omega(t)$ is given by:

$$\delta\omega(t) = \frac{d}{dt}(\phi_{NL}(t)) = -\frac{n_2\omega_0 L}{c}\frac{dI(t)}{dt} \tag{4}$$

An example of SPM is illustrated in Fig. 1(a), in which the pulse shape is given by a Gaussian distribution. Under the assumption that n_2 is positive, Eq. (4) indicates that the instantaneous frequency shifts to lower frequencies in the leading edge of the pulse and to higher frequencies in the trailing edge. The variation in the instantaneous frequency is illustrated by the solid red curve in Fig. 1(a). Equation (4) shows that the instantaneous frequency is proportional to the intensity gradient of the driving pulse $dI(t)/dt$. Consequently, shorter input pulses with a steeper slope $dI(t)/dt$ will result in more significant spectral broadening.

Similar to the time domain picture, the spatial intensity profile of the laser pulse leads to a spatial variation of $\phi_{NL}(x, y)$. For Gaussian beam profiles this variation resembles a quadratic phase profile (Fig. 1(b)), which causes the material to act as a positive lens. Analogous to the instantaneous frequency in Eq. (4) for the time-domain case, we can express the spatial frequency variation $\delta\mathbf{k}(x, y)$ due to self-focusing as:

$$\delta\mathbf{k}(x, y) = \nabla\phi_{NL}(x, y) = -\frac{n_2\omega_0 L}{c}\nabla I(x, y). \tag{5}$$

This expression shows that the induced wavefront curvature is proportional to the spatial intensity gradients. Large spatial gradients will thus cause significant self-focusing, which can lead to wavefront aberrations and result in optical damage to the optical components in the beamline [29,30].

Optics EXPRESS

Because SPM and self-focusing result from the same nonlinearity, they will always occur together. However, their dependence on temporal versus spatial intensity gradients provides a way to control the relative strength of the effects, which is the basis of the CASCADE concept. A loose focusing geometry minimizes spatial gradients and therefore limits self-focusing, while pulse compression between multiple SPM stages increases the temporal gradients to maximize spectral broadening.

3. Pulse compression in a loose focusing geometry

3.1. Experimental setup

The experimental setup is shown in Fig. 2. We use an Yb-based laser system (Pharos from Light Conversion) delivering 2 mJ, 170 fs pulses at a center wavelength of 1030 nm and a repetition rate of 1 kHz. The full-width-at-half-maximum (FWHM) beam diameter is 3.9 mm. The laser pulses are loosely focused in gas to induce nonlinear broadening with limited self-focusing, combined with chirped-mirror-based compression between passes. The pulses are first focused into a pressure-tunable argon gas cell by a concave mirror (5 m radius of curvature), and an another concave mirror is used to collimate the beam afterwards. The subsequent dispersion compensation is implemented using a pair of chirped mirrors (CMs) (GDD=−500 fs^2, UltraFast Innovations, CM39). To avoid additional nonlinear effects in the entrance and exit windows of the gas cell, we use 1 mm thin anti-reflection coated fused silica windows and place them close to the curved mirrors. The same loose focusing geometry is applied in the 2nd pass through a separate gas cell. The energy throughput of the system exceeds 90% and is mainly determined by the reflectivity of the mirrors.

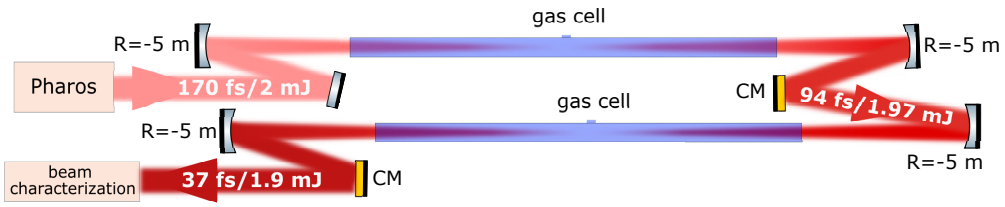

Fig. 2. Schematic of the setup: the laser output is loosely focused by the concave mirror R=-5 m into the argon gas cell, and subsequently collimated and compressed using chirped mirrors (CM). The 2nd pass uses a similar loose focusing geometry and CM compression.

3.2. Temporal pulse characterization: SHG-FROG

To characterize the temporal pulse profile and phase, SHG-FROG measurements (Mesa Photonics, LLC) are applied after each pass, with the results displayed in Fig. 3. The dark blue dashed traces in the left column of Fig. 3 show the broadened spectra after each pass as measured directly by the spectrometer. The reconstructed spectra from the SHG-FROG (solid blue traces) are in good agreement with these measurements. The broadened spectra are also consistent with calculations of the expected SPM (light blue traces). By comparing spectra, the B-integral (Eq. (2)) of the first and the second pass through 700 mbar argon is estimated at 1.3π and 1.7π, respectively. The nonlinear refractive index of argon at 700 mbar is taken to be $n_2(700\,mbar) = 0.9 \times 10^{-19} cm^2/W$ [31,32]). Without applying dispersion compensation between the passes, the total accumulated B-integral would have been 2.3π, i.e. 1.3 times less. Experiments at a higher gas pressure of 800 mbar in both cells (Fig. 3, bottom two rows) show a further increase in spectral broadening, but also more structured spectra.

The second column in Fig. 3 shows the pulse durations retrieved from the FROG reconstructions. After the first pass, pulse compression close to the Fourier transform limit (TL) is readily achieved,

Optics EXPRESS

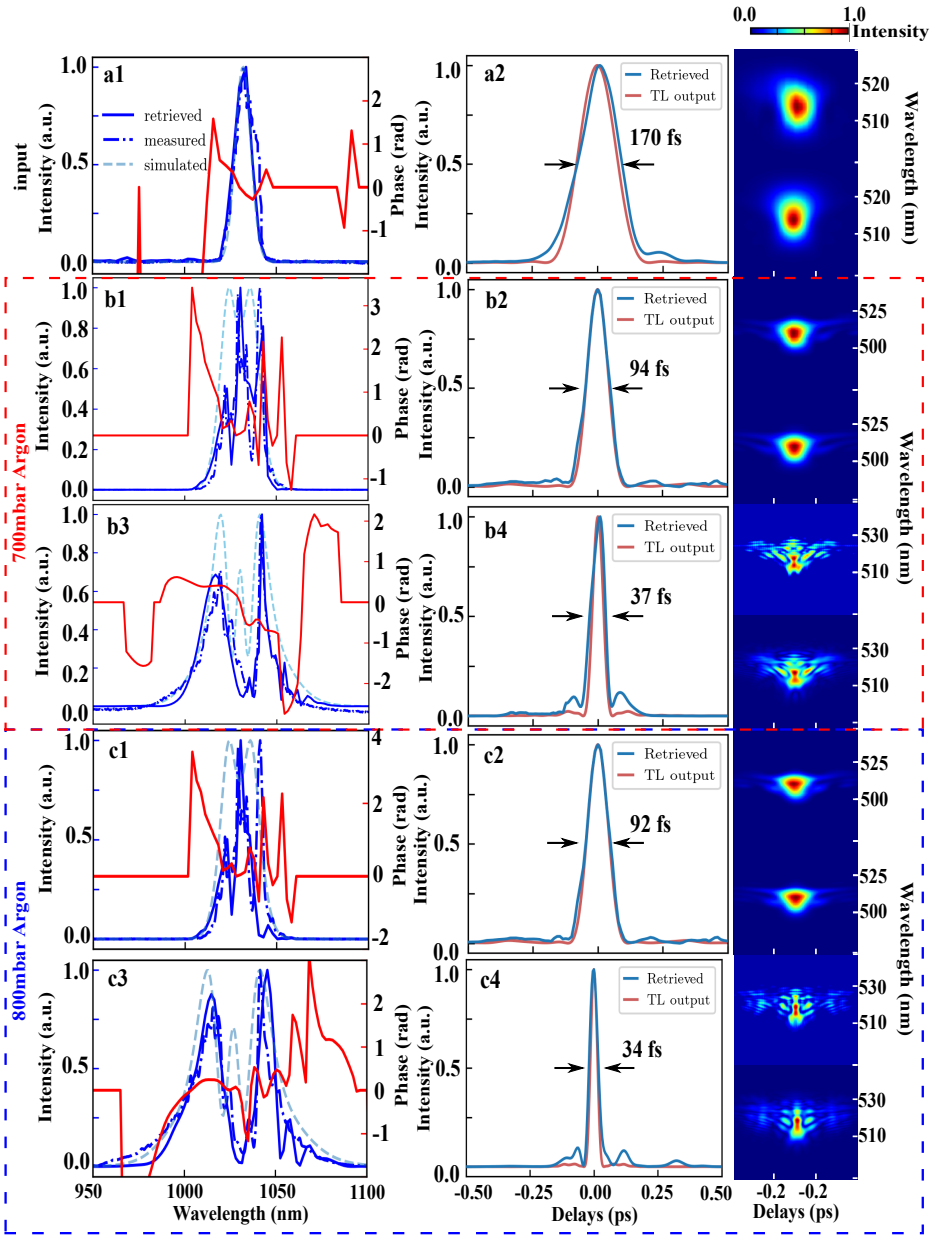

Fig. 3. SHG-FROG measurements and retrieved spectral fields and temporal pulse shapes for the input pulse (a1,a2), after the first gas cell and chirped mirrors (b1,b2,c1,c2), and after the second gas cell and additional chirped mirrors (b3,b4,c3,c4). For both gas cells, measurements were performed at Argon pressures of 700 mbar (b1-b4) and 800 mbar (c1-c4), respectively. The dark blue curves are the retrieved spectra from FROG measurements, and the dark blue dashed curves are measured spectra by spectrometer, and the light blue dashed curves are calculated spectra using Eq. (3). The red curves are the retrieved spectral phases. The third column shows the measured (top) and retrieved (bottom) FROG trace of each measurements, respectively.

Optics EXPRESS

and the temporal profiles are clean with only very minor pre- and post-pulses. After the second pass, near-transform-limited compression to 37 fs is still achieved, although some satellite pulses remain in the temporal profile, likely due to imperfect compensation of higher-order phase terms. Pulse compression to below the measured 37 fs can be achieved by further increasing the pressure inside the gas cells, along with fine-tuning the pass number in the chirped mirror compressor. At a pressure around 800 mbar in both cells, a slightly shorter pulse duration of 34 fs is retrieved (Fig. 3(c)).

The measured spectra for different gas pressures after the second cell are shown in Fig. 4(a). The bandwidth of the spectrum at −20 dB of the maximum value is plotted as grey points in Fig. 4(b). For pure SPM and assuming a linear dependence of n_2 on pressure, Eq. (4) predicts a linear trend [13,21,33], which is the case up to a pressure around 600 mbar. Beyond this pressure, the trend becomes nonlinear, indicating the growing influence of other mechanisms such as intensity changes induced by self-focusing during propagation.

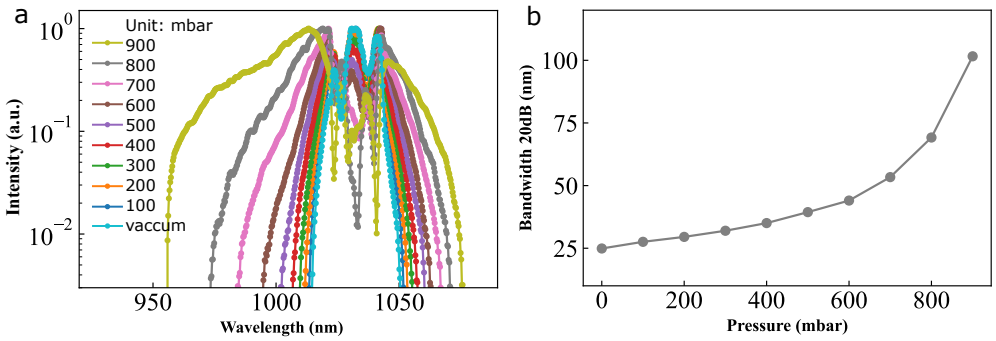

Fig. 4. a) Measured output spectra for different argon pressure in the second gas cell. b) Spectral width at 20 dB below maximum

3.3. *Spatial beam characterization: ptychographic wavefront sensing*

To characterize the spatial properties of the beam after the spectral broadening, ptychographic wavefront sensor (PWFS) measurements [25,26] are performed directly behind both gas cells. Such PWFS measurements retrieve high-resolution images of the full complex field (both amplitude and phase profiles). The fields are measured before the collimating mirror to accurately determine the curvature of the wavefront exiting the gas cell. To identify any wavelength dependence in the beam profiles, these PWFS measurements are performed for a series of wavelengths, which are selected using ultra-narrow bandpass filters (Laser Components HBP1063.1/1.8-25, HBP1030.2/1.2-25). The reconstructed fields after the two pulse compression cells for different wavelength components and two gas pressures are shown in Fig. 5.

The output after the first cell (Fig. 5(a1-a3)) shows no significant wavelength dependence of the wavefronts when using 700 mbar argon. Increasing gas pressure leads to a slight reduction in wavefront curvature (Fig. 5(b1-b3)) at the output due to self-focusing, while maintaining a Gaussian spatial profile across the spectrum. Using 700 mbar argon in the CASCADE, pulse compression after the first cell results in 94 fs pulse duration, which leads to increased nonlinear effects in the second cell as propagation conditions are kept nominally identical to the first pass. The PWFS measurements after the second cell (Fig. 5(c1-c5,d1-d5) confirm this, with the wavefronts showing more pronounced variations in curvature, and a stronger dependence on gas pressure. As a consequence of the increased SPM, we could measure at two more wavelength components near the edges of the output spectrum. Note that these wavelength components were generated via SPM and were not in the input spectrum.

Optics EXPRESS

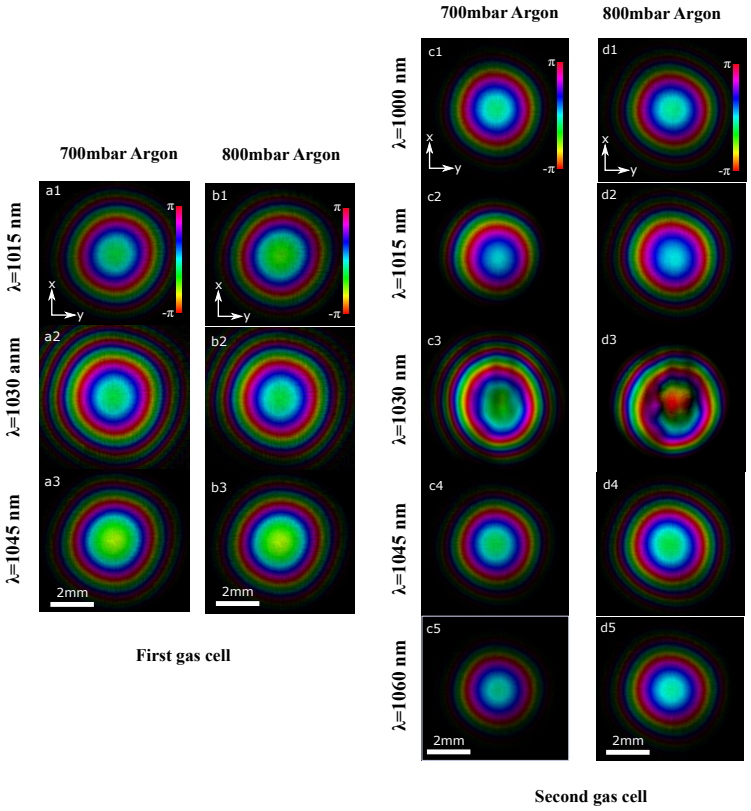

Fig. 5. Reconstructed probe beams after a-b. first gas cell and c-d. second gas cell under 700 mbar and 800 mbar argon, respectively. Color encodes phase (see scale bar), and brightness represents field amplitude.

Increasing the gas pressure to 800 mbar (Fig. 5(d)) leads to particularly significant beam distortions at 1030 nm, including intensity modulations across the beam, and the nonlinear effects at 1015 nm and 1045 nm start to deteriorate the output wavefront as well. At this pressure, the input power is just below the critical power, $P_{in} = 0.87P_{cr}$, which will lead to multiphoton ionization and plasma generation [34]. The distortion of beam wavefronts under such significant nonlinear effects are to be expected.

Knowing both the amplitude and phase profiles at the plane of the PWFS allows us to numerically propagate the beams to any plane, enabling us to assess beam quality. Starting with the measured wavefronts, we first remove the quadratic phase to get the transverse field distribution $E(x, y)$ corresponding to a focal length of 2.5 m before the second CASCADE gas cell. Subsequently, a phase curvature corresponding to a lens with a focal length $f = 30\,cm$ is numerically added to evaluate beam propagation quality under typical experimental conditions. This beam propagation [35] in the z-direction over a distance dz can be described as:

$$E(x, y, z + dz) = \mathcal{F}^{-1}\{\mathcal{F}\{E(x, y, z)exp(ik(x^2 + y^2)/2f)\}H(k_x, k_y, dz)\} \tag{6}$$

where $\mathcal{F}$ and $\mathcal{F}^{-1}$ denote forward and inverse 2D Fourier transforms. The propagation transfer function $H(k_x, k_y, dz)$ is given by:

$$H(k_x, k_y, dz) = \exp(i\sqrt{k^2 - k_x^2 - k_y^2}dz) \tag{7}$$

Optics EXPRESS

where k is the magnitude of the wavevector of the propagated field, and k_x and k_y are the transverse components of the wavevector. The transfer function in Eq. (7) describes linear propagation. In our calculations, we set dz to 1 mm, smaller than the Rayleigh length (30 mm at 1060 nm), to obtain a detailed view of propagation through the focal region.

Using this approach we can construct side-view images of the beam propagation through the focus (Fig. 6(a,b)), where the white dashed lines indicate the position of lens focus. The divergence and focal positions for each wavelength can be clearly identified, and a tight focus is observed in the cross section, without major influence of astigmatism or other wavefront aberrations. The limited variation in focal position across wavelengths indicates the absence of chromatic aberration in the pulse compression process.

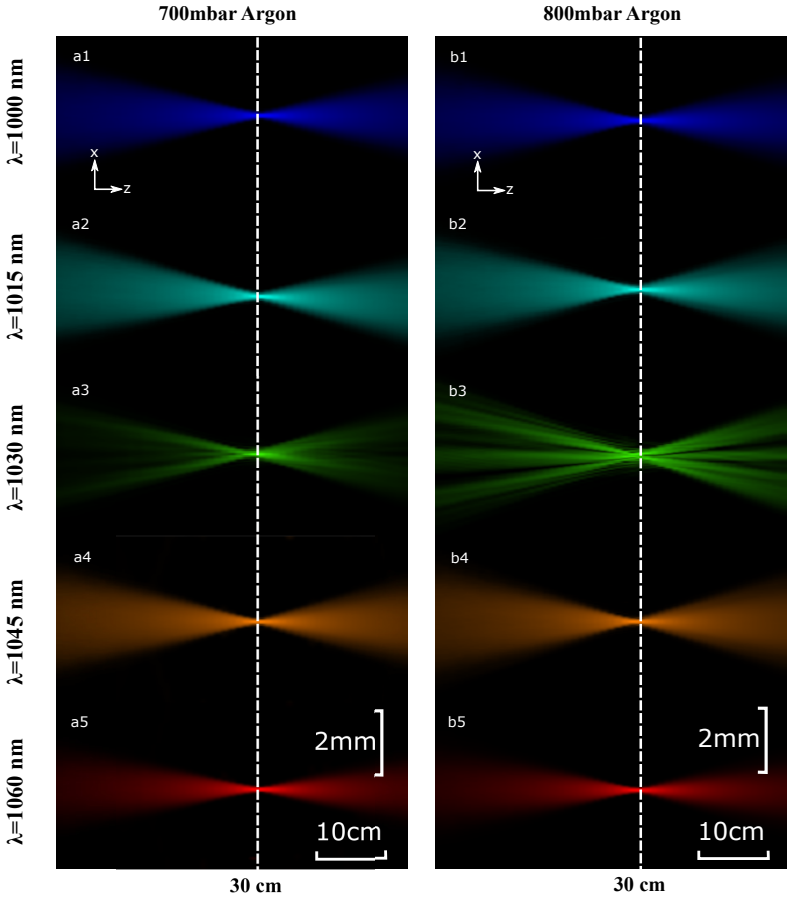

Fig. 6. Numerical forward propagation of the experimentally retrieved complex fields at multiple wavelengths. a1-a5) Numerically reconstructed xz-plane side-views of the beams from Fig. 5(c) (propagation from left to right). b1-b5) Numerically reconstructed xz-plane side-views of the beams from Fig. 5(b). The white dashed lines indicate the physical location of the focus position.

Propagating the most intense wavelengths beams to a common focal plane enables us to investigate the spatiospectral properties and focus quality of the beam. Figure 7(a4-a6 and b4-b6) show the intensity distributions for different wavelength components. The strong nonlinear effects during spectral broadening, especially for 800 mbar argon pressure, lead to the formation of a non-Gaussian focused beam at the input wavelength of 1030 nm, as shown in Fig. 7(b5). At

Optics EXPRESS

700 mbar pressure, the incoherent addition of all wavelength components gives a well-formed polychromatic focus, with the FWHM beam diameter of approximately 306.8 um (Fig. 7(a1)). However, small wavelength-dependent differences in spot shape are already visible. At 800 mbar pressure, sidelobes and wavelength-dependent focusing differences significantly affect the quality of the polychromatic focus (Fig. 7(b3)).

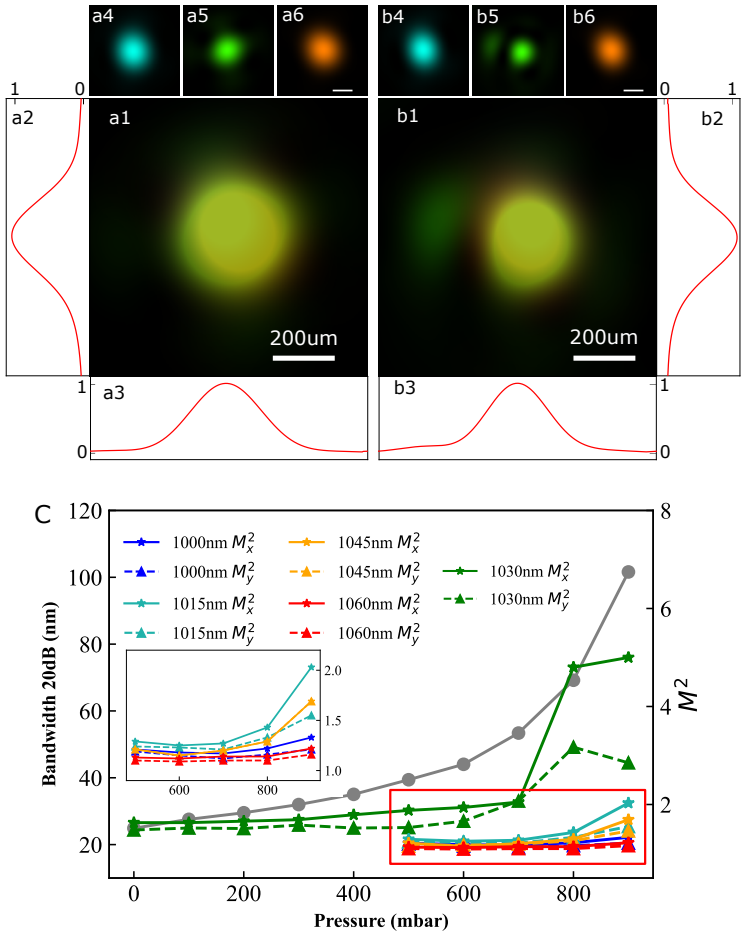

Fig. 7. Intensity profile of the polychromatic focus summed over three central wavelength beams after a1) 700 mbar and b1) 800 mbar argon filled CASCADE, respectively. 1D intensity of the polychromatic focus for a2-a3) 700 mbar and b2-b3) 800 mbar argon filled CASCADE, respectively. The sub-figures a4-a6) and b4-b6) show the color coded monochromatic (blue: 1015 nm, green: 1030 nm, orange: 1045 nm) intensity plots of corresponding focus, and the scaled bar represents 200 um. c) Beam quality parameter M^2 as determined for different wavelength components separately. The inset figure shows the enlarged view of the red area, to better visualize the M^2 values for the wavelengths towards the edge of the spectrum. The bandwidth of the broadened spectrum at −20 dB of the maximum value is plotted as grey points, which refer to the left y-axis.

To connect our PWFS results to other common methods for beam quality analysis, we retrieve M^2 values from the measured complex wavefronts [25] over a range of gas pressures. Starting from the reconstructed complex-valued probes at 1030 nm, we linearly propagate these fields through a focus and subsequently calculate M_x^2 and M_y^2. The retrieved values as a function of argon

Optics EXPRESS

pressure are shown in Fig. 7(c). Starting from an input laser beam with $M^2 = 1.11 \times 1.11$, the beam quality factor maintains acceptable values of $M^2 = 2$ after the two-stage post-compression for argon pressure up to 700 mbar. We attribute the difference in beam quality of the two axes to the slight astigmatism in the beam caused by the focusing mirrors, leading to a small different nonlinearity. The inset figure in Fig. 7(c) also shows the beam quality of spectral components towards the edges of the bandwidth. Interestingly, these components consistently maintain a high beam quality throughout the spectral broadening process, even at gas pressures up to 900 mbar. In contrast, the beam quality at the center wavelength severely degrades above 700 mbar, showing significant intensity modulations and phase distortions (Fig. 5(d3)), caused by excessive nonlinear effects [14] at these higher gas pressures, which would eventually lead to optical breakdown [34].

The high beam quality at the outer spectral ranges can be explained by the SPM mechanism, as these wavelengths are mainly generated inside the (second) gas cell. As these wavelength components only appear around the focus, they experience much less nonlinear propagation effects and associated self-focusing and other beam distortion effects.

In the presented double-pass configuration, using our specific beam parameters and focusing geometry, we therefore conclude that maintaining sufficient beam quality across the spectrum requires an argon pressure below 700 mbar, and therefore the achievable compressed pulse duration is limited to 37 fs. Even though shorter pulse durations are obtained at higher pressure, the (wavelength-dependent) reduction in beam quality will likely reduce the applicability of such pulses in strong-field experiments.

We confirm this expectation by using the compressed pulses for high-harmonic generation (HHG) in a gas jet geometry. To achieve a Fourier-limited pulse at different CASCADE pressures, we adjusted the number of bounces on the CMs and confirmed the pulse duration through FROG measurements. In addition to optimizing the pulse compression, we adjusted other HHG generation parameters independently, such as gas backing pressure and lens position, to maximize HHG brightness. When focusing the pulses into a 0.6 mm wide argon jet (around 4 bar backing pressure), using a 30 cm focal length lens, we observe optimal HHG for an argon pressure of 620 mbar in the compression cells. Increasing the pressure to 750 mbar results in a 7% reduction in HHG yield, which we attribute to the reduced overall laser beam quality.

An extension towards shorter pulse durations will therefore require an increase in SPM without increasing the spatial nonlinearities such as self-focusing. This can be achieved by an even looser focusing geometry, to reduce the spatial gradients (Eq. (5)) while maintaining temporal gradients (Eq. (4)). Alternatively, adding more passes through the nonlinear medium at constant or even slightly lower gas pressure will have a similar effect. Including pulse compression after each stage will then significantly improve the SPM-to-self-focusing ratio, as it increases the temporal gradients before subsequent broadening. This approach was recently shown to work very effectively [24]. Such intermediate compression is more challenging to incorporate in multipass cell configurations, but can be achieved e.g. by using chirped cavity mirrors [36,37].

4. Conclusions

Using a double-pass CASCADE scheme, we demonstrate post-compression of 2 mJ 170 fs Yb ion-doped laser pulses to 37 fs with 90% overall flux efficiency, while maintaining good beam quality across the full spectrum. Specifically, we use SHG-FROG and PWFS measurements to characterize the compressed pulses in both the temporal and spatial domain. This approach provides a detailed view on the results of the nonlinear effects in each broadening stage, and it enables a determination of optimum working conditions for the pulse compression system in terms of pulse duration, beam quality and system complexity. Specifically, we note the importance of wavelength-resolved wavefront characterization, as highlighted by our observations in Fig. 5. While an averaged wavefront and beam profile may show acceptable behavior, we find that the nonlinear propagation can lead to strong aberrations at specific wavelength components,

Optics EXPRESS

especially those already present in the input spectrum. This effect may lead to significant spatiotemporal coupling upon focusing, affecting the efficiency and reproducibility in strong-field experiments.

While a similar approach can be taken to characterize multipass cell or fiber-based compression systems, we focused on a particularly simple implementation of the CASCADE-type scheme using only double-pass compression. Our measurements confirm that these systems indeed enable effective broadening via SPM while limiting self-focusing, and have favourable scaling properties towards higher pulse energy.

Appendix: simulation for numerical back-propagation

In addition to the forward propagation to study the focusing properties of the compressed beam, a similar propagation approach can also be used for backward propagation, to study the beam as it emerges from the gas cells. A complete analysis would require solving the nonlinear time-dependent Schrodinger equation in 3D, which is a computationally challenging task. We employ a more limited approach, which still provides insight into the main operating conditions of the CASCADE system.

To include the effect of self-focusing in the beam reconstruction inside the gas cell, we numerically propagate the PWFS reconstructions backwards through the nonlinear medium using a split-step approach [38]. Starting with a transverse field distribution $E(x, y)$, propagation in the z-direction over a distance dz can be described as:

$$E(x, y, z + dz) = \mathcal{F}^{-1}\{\mathcal{F}\{E(x, y, z)\}H(k_x, k_y, dz)\exp(i\phi_{NL}(x, y))\} \tag{8}$$

where $\mathcal{F}$ and $\mathcal{F}^{-1}$ denote forward and inverse 2D Fourier transforms. The transfer function is given in Eq. (7). The nonlinearity is included by multiplying the propagated field with a phase term including $\phi_{NL}(x, y)$ in the Fourier domain in Eq. (8). The nonlinear phase can be

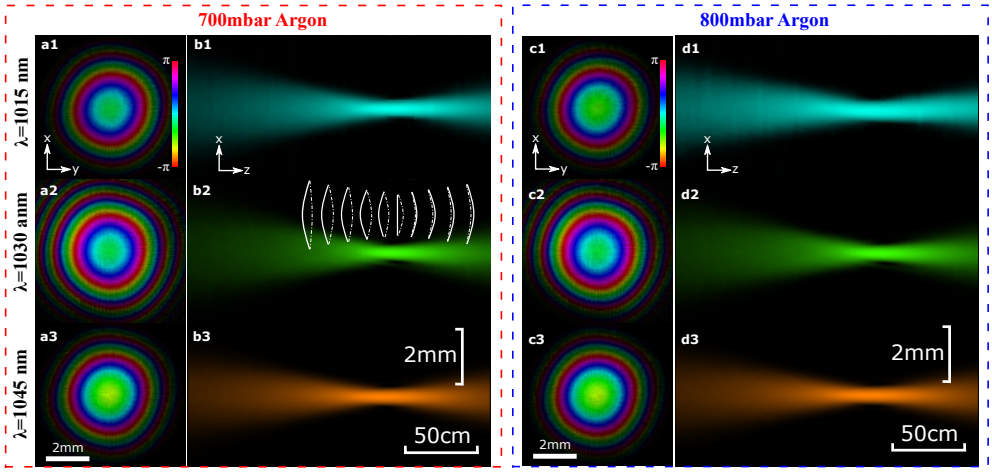

Fig. 8. Spatial beam characterization after the first gas cell. a1-a3) Ptychographic wavefront reconstructions at 700 mbar argon pressure, at wavelengths of 1015 nm, 1030 nm and 1045 nm, respectively. Color encodes phase (see scale bar), and brightness represents field amplitude. b1-b3) Numerically reconstructed xz-plane side-views of the beams from a) propagation from right to left. The inset in b2 schematically shows the wavefront curvature for linear propagation (solid lines) and the contribution of self-focusing (dash-dotted lines, not to scale). c1-c3) Ptychographic wavefront reconstructions at 800 mbar argon pressure. d1-d3) Numerically reconstructed xz-plane side-views of the beams from c.

Optics EXPRESS

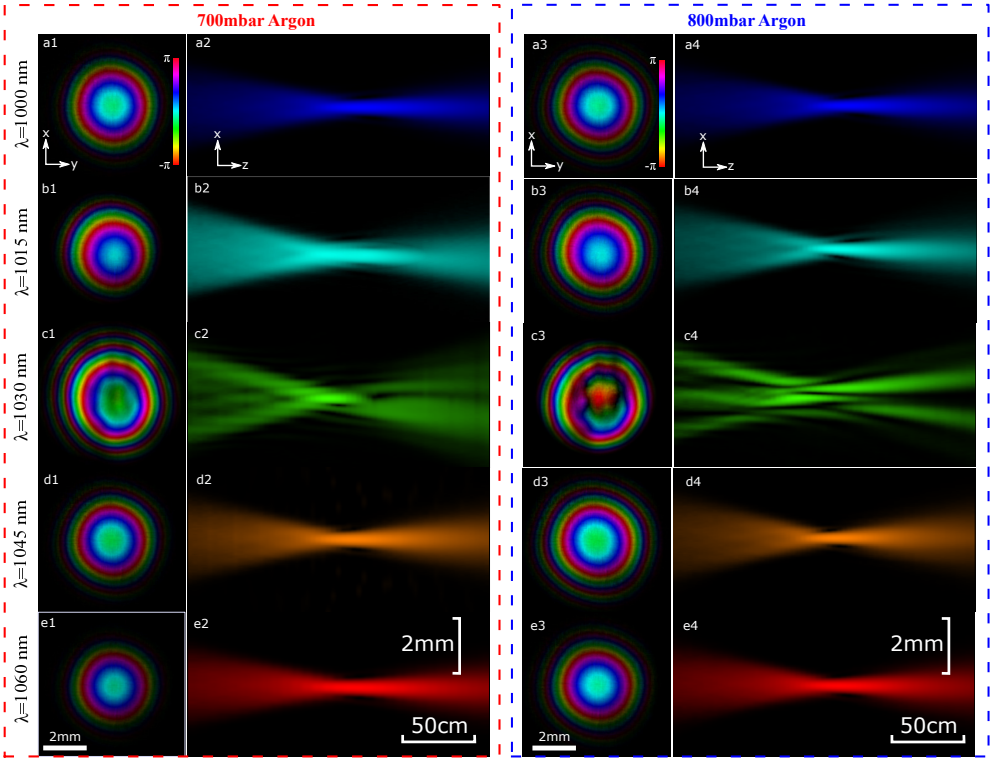

Fig. 9. Spatial beam characterization after the second gas cell. a1-a5) Ptychographic wavefront reconstructions at 700 mbar argon pressure at five different wavelength components. Color encodes phase (see scale bar), and brightness represents field amplitude. b1-b5) Numerically reconstructed xz-plane side-views of the beams from a) propagation from right to left. c1-c5) Ptychographic wavefront reconstructions at 800 mbar argon pressure. d1-d5) Numerically reconstructed xz-plane side-views of the beams from c.

calculated for a given intensity profile using Eq. (2), which however varies during propagation. To approximate the nonlinear propagation, Eq. (8) is evaluated for a series of steps, where the step size dz is sufficiently small to approximate the intensity profile close to constant over this length [39]. The phase $\phi_{NL}(x, y)$ is calculated at each step and included in the field propagation via Eq. (8). In our calculations dz is chosen as $dz = -5\,cm$, corresponding to half of the Rayleigh length.

Using this approach we can construct side-view images of the beam propagation through the gas cell (Fig. 8(b,d)). Because of the limitations of the approach, these images do not contain information about the nonlinear frequency conversion, but are only intended to assess the importance of self-focusing in the beam propagation. Of course, the wavelength components at 1015 and 1045 nm in Fig. 8 are generated around the focus, and therefore propagating them to before the focal point is not realistic. However, the relative focus positions as they are influenced by the self-focusing effect can be determined through this approach, which is a major design parameter for the CASCADE system.

For the first pass, we find only limited influence of self-focusing, with the beam propagation only slightly deviating from linear Gaussian beam propagation. To illustrate the effect of self-focusing, Fig. 8(b2) has an inset showing the wavefront for linear propagation (solid lines) as well as the induced wavefront change due to self-focusing (dash-dotted lines). As the beam

Optics EXPRESS

converges towards the focus, the increased intensity leads to a stronger influence of self-focusing. For this first pass example, the maximum induced phase lag near the focal plane is estimated at 0.06 rad via Eq. (2). Overall the output from the first gas cell shows no significant wavelength dependence of the wavefronts. Increasing gas pressure leads to a slight reduction in wavefront curvature at the output due to self-focusing, while maintaining a Gaussian spatial profile across the spectrum.

Using 700 mbar argon in the CASCADE, our pulse compression after the first cell results in 94 fs pulse duration, which results in increased nonlinear effects in the second cell as propagation conditions are kept nominally identical to the first pass. As a consequence of the increased SPM, we could measure at two more wavelength components near the edges of the output spectrum. Note that these wavelength components were generated via SPM and were not in the input spectrum. Therefore, propagating them backwards through the cell as shown in Fig. 9(b,d) is mainly done to characterize their propagation after the focus in comparison to the other wavelength components. A striking observation is that at the center wavelength of 1030 nm, propagation clearly deviates from linear Gaussian behavior with minor modifications, but shows additional diffraction effects. As our model only includes linear propagation and self-focusing via Eq. (2), the exact beam properties near the focus cannot be reliably reconstructed in this way. Given that the input beam has a clean Gaussian intensity and wavefront (see Fig. 8) that does not match the propagation result in Fig. 9(b3), we can conclude that additional nonlinear effects influence the propagation in the second cell. While more detailed propagation simulations can include such effects [24,30,34], this working regime is not suitable for a stable pulse compression system, and the present PWFS data and these basic simulations can be used to identify the limits. Interestingly, the wavelengths towards the edge of the spectrum, which are produced inside the cell, do display smooth beam profiles and wavefronts that allow high-quality focusing.

Funding. Toegepaste en Technische Wetenschappen, NWO (19405, P16-08); European Research Council (864016).

Acknowledgments. FZ, MG and SW acknowledge support from the European Research Council (ERC-CoG project 3D-VIEW, 864016). AP, JS and SW acknowledge funding from the Dutch Research Council NWO (Perspectief program LINX, P16-08). AK and SW acknowledge funding from NWO VICI project 19405. This work was carried out at ARCNL, a public-private partnership between the University of Amsterdam (UvA), Vrije Universiteit Amsterdam (VU), Rijksuniversiteit Groningen (RUG), the Dutch Research Council (NWO), and the semiconductor equipment manufacturer ASML.

Disclosures. The authors declare no conflicts of interest.

Data availability. All data underlying the results of this paper may be obtained from the authors upon reasonable request.

References

1. G. Mourou, "Nobel lecture: Extreme light physics and application," Rev. Mod. Phys. **91**(3), 030501 (2019).
2. H. Fattahi, H. G. Barros, M. Gorjan, *et al.*, "Third-generation femtosecond technology," Optica **1**(1), 45–63 (2014).
3. T. Brabec and F. Krausz, "Intense few-cycle laser fields: Frontiers of nonlinear optics," Rev. Mod. Phys. **72**(2), 545–591 (2000).
4. C. Jauregui, J. Limpert, and A. Tünnermann, "High-power fibre lasers," Nat. Photonics **7**(11), 861–867 (2013).
5. D. Rand, D. Miller, D. J. Ripin, *et al.*, "Cryogenic yb 3+-doped materials for pulsed solid-state laser applications," Opt. Mater. Express **1**(3), 434–450 (2011).
6. A. Dubietis, G. Jonušauskas, and A. Piskarskas, "Powerful femtosecond pulse generation by chirped and stretched pulse parametric amplification in bbo crystal," Opt. Commun. **88**(4-6), 437–440 (1992).
7. R. Klas, W. Eschen, A. Kirsche, *et al.*, "Generation of coherent broadband high photon flux continua in the xuv with a sub-two-cycle fiber laser," Opt. Express **28**(5), 6188–6196 (2020).
8. B. Zhu, Z. Fu, Y. Chen, *et al.*, "Spatially homogeneous few-cycle compression of Yb lasers via all-solid-state free-space soliton management," Opt. Express **30**(2), 2918–2932 (2022).
9. C. M. Heyl, M. Seidel, E. Escoto, *et al.*, "High-energy bow tie multi-pass cells for nonlinear spectral broadening applications," J. Phys. Photonics **4**(1), 014002 (2022).
10. Y. Pfaff, G. Barbiero, M. Rampp, *et al.*, "Nonlinear pulse compression of a 200 mJ and 1 kw ultrafast thin-disk amplifier," Opt. Express **31**(14), 22740–22756 (2023).
11. Y.-G. Jeong, R. Piccoli, D. Ferachou, *et al.*, "Direct compression of 170-fs 50-cycle pulses down to 1.5 cycles with 70% transmission," Sci. Rep. **8**(1), 11794 (2018).

Optics EXPRESS

12. M. Kaumanns, D. Kormin, T. Nubbemeyer, *et al.*, "Spectral broadening of 112 mj, 1.3 ps pulses at 5 khz in a lg 10 multipass cell with compressibility to 37 fs," Opt. Lett. **46**(5), 929–932 (2021).
13. V. S. Staels, E. C. Jarque, D. Carlson, *et al.*, "Numerical investigation of gas-filled multipass cells in the enhanced dispersion regime for clean spectral broadening and pulse compression," Opt. Express **31**(12), 18898–18906 (2023).
14. S. Tóth, R. S. Nagymihály, I. Seres, *et al.*, "Single thin-plate compression of multi-TW laser pulses to 3.9 fs," Opt. Lett. **48**(1), 57–60 (2023).
15. M. Nisoli, S. Stagira, S. De Silvestri, *et al.*, "A novel-high energy pulse compression system: generation of multigigawatt sub-5-fs pulses," Appl. Phys. B: Lasers Opt. **65**(2), 189–196 (1997).
16. Z. Pi, H. Kim, and E. Goulielmakis, "Petahertz-scale spectral broadening and few-cycle compression of yb: Kgw laser pulses in a pressurized, gas-filled hollow-core fiber," Opt. Lett. **47**(22), 5865–5868 (2022).
17. L. Chou, H. Hung, A. Liu, *et al.*, "Widely tunable femtosecond sources with continuously tailorable bandwidth enabled by self-phase modulation," Laser Photonics Rev. **17**(7), 2200297 (2023).
18. C. Lu, Y. Tsou, H. Chen, *et al.*, "Generation of intense supercontinuum in condensed media," Optica **1**(6), 400–406 (2014).
19. A. Viotti, M. Seidel, E. Escoto, *et al.*, "Multi-pass cells for post-compression of ultrashort laser pulses," Optica **9**(2), 197–216 (2022).
20. M. Hanna, F. Guichard, N. Daher, *et al.*, "Nonlinear optics in multipass cells," Laser Photonics Rev. **15**(12), 2100220 (2021).
21. M. Ueffing, S. Reiger, M. Kaumanns, *et al.*, "Nonlinear pulse compression in a gas-filled multipass cell," Opt. Lett. **43**(9), 2070–2073 (2018).
22. A. Viotti, C. Li, G. Arisholm, *et al.*, "Few-cycle pulse generation by double-stage hybrid multi-pass multi-plate nonlinear pulse compression," Opt. Lett. **48**(4), 984–987 (2023).
23. S. Goncharov, K. Fritsch, and O. Pronin, "Few-cycle pulse compression and white light generation in cascaded multipass cells," Opt. Lett. **48**(1), 147–150 (2023).
24. M. Tsai, A. Liang, C. Tsai, *et al.*, "Nonlinear compression toward high-energy single-cycle pulses by cascaded focus and compression," Sci. Adv. **8**(31), eabo1945 (2022).
25. M. Du, L. Loetgering, K. S. E. Eikema, *et al.*, "Measuring laser beam quality, wavefronts, and lens aberrations using ptychography," Opt. Express **28**(4), 5022–5034 (2020).
26. M. Du, X. Liu, A. Pelekanidis, *et al.*, "High-resolution wavefront sensing and aberration analysis of multi-spectral extreme ultraviolet beams," Optica **10**(2), 255–263 (2023).
27. L. Loetgering, S. Witte, and J. Rothhardt, "Advances in laboratory-scale ptychography using high harmonic sources," Opt. Express **30**(3), 4133–4164 (2022).
28. N. Daher, F. Guichard, S. W. Jolly, *et al.*, "Multipass cells: 1d numerical model and investigation of spatio-spectral couplings at high nonlinearity," J. Opt. Soc. Am. B **37**(4), 993–999 (2020).
29. S. A. Akhmanov, A. P. Sukhorukov, and R. V. Khokhlov, "Self-focusing and diffraction of light in a nonlinear medium," Sov. Phys. Usp. **10**(5), 609–636 (1968).
30. R. W. Boyd, S. G. Lukishova, and Y. R. Shen, *Self-focusing: Past and present: Fundamentals and prospects* (Springer, 2009).
31. E. Nibbering, G. Grillon, M. A. Franco, *et al.*, "Determination of the inertial contribution to the nonlinear refractive index of air, n 2, and o 2 by use of unfocused high-intensity femtosecond laser pulses," J. Opt. Soc. Am. B **14**(3), 650–660 (1997).
32. M. Shaw, C. Hooker, and D. Wilson, "Measurement of the nonlinear refractive index of air and other gases at 248 nm," Opt. Commun. **103**(1-2), 153–160 (1993).
33. D. Shelton, "Nonlinear-optical susceptibilities of gases measured at 1064 and 1319 nm," Phys. Rev. A **42**(5), 2578–2592 (1990).
34. M. Mlejnek, E. Wright, and J. Moloney, "Femtosecond pulse propagation in argon: A pressure dependence study," Phys. Rev. E **58**(4), 4903–4910 (1998).
35. J. D. Schmidt, *Numerical simulation of optical wave propagation with examples in MATLAB* (Spie, 2010).
36. L. Silletti, A. Bin Wahid, E. Escoto, *et al.*, "Dispersion-engineered multi-pass cell for single-stage post-compression of an ytterbium laser," Opt. Lett. **48**(7), 1842 (2023).
37. M. Benner, M. Karst, C. Amaya Mendez, *et al.*, "Concept of enhanced frequency chirping for multi-pass cells to improve the pulse contrast," J. Opt. Soc. Am. B **40**(2), 301 (2023).
38. G. P. Agrawal, *Nonlinear Fiber Optics* (Elsevier, 2013), 5th ed.
39. R. W. Boyd, A. L. Gaeta, and E. Giese, *Nonlinear optics, in Springer Handbook of Atomic, Molecular, and Optical Physics*, (Springer, 2008), pp. 1097–1110.